COMPARATIVE PHYSICOCHEMICAL AND OPTICAL CHARACTERIZATION OF CUO AND SNO_2 NANOPARTICLES IN ALCOHOL SOLVENTS

Anil Kumar[1], Swati[2], Niharika[3]*
[1]Applied Science Department, Bharati Vidyapeeth's College of Engineering, New Delhi, India
[2]Department of Chemistry, Baba Mastnath University, Rohtak, Haryana, India
[3]Research Scholar, Department of Chemistry, Baba Mastnath University, Rohtak, Haryana, India
***Corresponding author Email: niharikaniharika985@gmail.com**

ABSTRACT

This study presents a comparative physicochemical and optical characterization of CuO and SnO_2 nanoparticles synthesized via co-precipitation and hydrothermal methods, respectively. Comprehensive analysis using XRD, FESEM, EDX, and FTIR confirms monoclinic CuO (15 nm crystallite size) with sulfur impurities and phase-pure rutile SnO_2 evolving from SnO intermediates upon calcination (300-450°C). Solvent-dependent UV-Vis spectroscopy reveals significant quantum confinement effects, yielding direct band gaps of 3.00-3.87 eV (CuO) and 3.75-5.33 eV (SnO_2) across ethanol-to-hexanol series, far exceeding bulk values (1.5-1.9 eV CuO, 3.6 eV SnO_2). Photoluminescence studies (290 nm excitation) demonstrate near-band-edge emissions (348-359 nm CuO, 315-321 nm SnO_2) with ethanol optimizing CuO and propanol maximizing SnO_2 intensities. Time-resolved measurements confirm bi-exponential decay (τ_avg: 2.32-5.22 ns) for SnO_2, revealing solute-solvent interactions modulating carrier lifetimes through dielectric permittivity gradients. These findings establish alcohol chain length as a critical parameter for tailoring metal oxide nanoparticle optoelectronic properties, offering insights for sensor and photocatalyst applications.

Keywords: CuO nanoparticles, SnO_2 nanoparticles, quantum confinement, solvent-dependent band gap, photoluminescence, time-resolved fluorescence, XRD analysis, FESEM morphology, solute-solvent interactions, dielectric modulation

1. INTRODUCTION

Metal oxide nanoparticles, particularly CuO and SnO_2, have garnered significant attention due to their tunable optoelectronic properties enabling applications in gas sensors, photocatalysis, and optoelectronic devices [Baco et al., 2012][Dar et al., 2008]. The quantum confinement effect in nanomaterials dramatically alters their band gap energies, with CuO exhibiting p-type semiconducting behavior (bulk $E_g \approx 1.5$-1.9 eV) and SnO_2 demonstrating n-type characteristics (bulk $E_g \approx 3.6$ eV), both showing substantial blue-shifts upon nanosizing [Sagadevan & Podder, 2016][Gu et al., 2004]. While extensive literature documents size-dependent optical properties, the influence of solvent environment on post-synthesis dispersion remains underexplored despite critical implications for practical device integration [Horti et al., 2020][Khoza et al., 2012].

Traditional characterization approaches often overlook solute-solvent interactions that modulate dielectric screening, hydrogen bonding, and solvation shell formation around nanoparticles. Primary alcohols (C_2-C_6) present a systematic dielectric gradient (ε_r: 24.5→11.6) ideal for probing these effects, where ethanol maximizes polarity while hexanol approaches non-polar behavior [Shnain et al., 2022][Zhang & Liu, 2010]. Prior studies report solvent-induced band gap variations in individual systems—CuO showing ethanol stabilization [El-Trass et al., 2012] and SnO_2 exhibiting propanol-enhanced emission [Bhuvaneshwari et al., 2016]—yet lack direct comparative analysis across homologous series that could reveal structure-property correlations [Zayyoun et al., 2016][Gnanam & Rajendran, 2011].

This study addresses these gaps through systematic physicochemical and time-resolved optical characterization of co-

precipitation-derived CuO (15 nm) and hydrothermally-prepared SnO_2 (phase-pure at 450°C) nanoparticles dispersed in ethanol through hexanol [Phiwdang et al., 2013][Volanti et al., 2008]. Beyond confirming expected quantum confinement (E_g,CuO: 3.00-3.87 eV; E_g,SnO_2: 3.75-5.33 eV), we demonstrate differential solvent optimization—ethanol for CuO excitons, propanol for SnO_2 lifetimes (τ_avg up to 5.22 ns)—attributed to dielectric matching and surface trap modulation [Das et al., 2006][Senthil Kumar et al., 2006]. These findings, contrasting aggregation-dominated interpretations [Mageshwari et al., 2013], establish alcohol chain length as a synthetic handle for tailoring metal oxide nanophotonics [Diallo et al., 2015][Vidyasagar et al., 2012].

2. LITERATUER REVIEW

Synthesis Methods and Structural Properties

Co-precipitation remains the dominant route for CuO nanoparticles due to its simplicity and scalability, yielding monoclinic phase materials with crystallite sizes typically 10-30 nm as confirmed by XRD matching JCPDS 48-1548 [Phiwdang et al., 2013][Sagadevan & Podder, 2016]. Sulfur impurities from precursor residues, evident in EDX and FTIR (SO_4^{2-} at ~1111 cm^{-1}), are commonly reported though rarely quantified [El-Trass et al., 2012]. Hydrothermal synthesis followed by calcination (300-500°C) effectively controls SnO_2 phase evolution from orthorhombic SnO intermediates (JCPDS 06-0395) to pure rutile tetragonal structure (JCPDS 41-1445), with Scherrer analysis revealing crystallite growth from oxygen vacancy annealing [Ristić et al., 2002][Bargougui et al., 2015]. FESEM consistently shows agglomeration in both systems, with CuO exhibiting mixed irregular/rod morphology (~30 nm diameter) and SnO_2 displaying calcination-dependent grain coarsening [Volanti et al., 2008][Gnanam & Rajendran, 2011].

Quantum Confinement and UV-Vis Spectroscopy

Nanosizing induces dramatic band gap widening beyond bulk limits: CuO from 1.5-1.9 eV to 2.1-4.0 eV, SnO_2 from 3.6 eV to 3.8-5.5 eV, validated by Tauc plots assuming direct allowed transitions [$(\alpha h\nu)^2$ vs $h\nu$] [Gu et al., 2004][Das et al., 2006]. Solvent effects on absorption edges remain contentious—early reports attributed blue-shifts to aggregation [Mageshwari et al., 2013], while recent studies demonstrate dielectric screening and hydrogen bonding stabilization in primary alcohols [Horti et al., 2020][Zayyoun et al., 2016]. CuO shows pronounced spectral broadening from Cu^{2+} d-d transitions modulated by alcohol chain length, contrasting SnO_2's sharper excitonic features [Dara et al., 2024][Senthil Kumar et al., 2006].

Photoluminescence Mechanisms and Defect States

Near-band-edge PL dominates both systems under 290 nm excitation: CuO emits at 340-360 nm from electron-hole recombination, SnO_2 at 310-330 nm, with defect bands (~470 nm CuO oxygen vacancies, Sn interstitials) revealing surface trap densities [Bhuvaneshwari et al., 2016][Dar et al., 2008]. Solvent polarity critically influences intensity—ethanol maximizes CuO via optimal solvation shell dielectric matching (ε_r = 24.5), while propanol enhances SnO_2 through reduced non-radiative decay [Khoza et al., 2012][Shnain et al., 2022]. Time-resolved TCSPC studies confirm bi-exponential decays (τ_1: shallow traps ~25 ps, τ_2: deep traps 2-5 ns), with average lifetimes correlating inversely with alcohol viscosity and dielectric constant [Tamrakar & Bisen, 2013][Bouaine et al., 2007].

Solute-Solvent Interactions and Research Gaps

Dielectric gradient across C_2-C_6 alcohols (ε_r: 24.5→11.6) systematically modulates nanoparticle solvation shells, altering local refractive index and Stokes shifts as evidenced by wavelength-dependent emission tuning [Zhang & Liu, 2010][Kose et al., 2008]. While individual CuO [Diallo et al., 2015] and SnO_2 [Baco et al., 2012] solvent studies exist, comparative analyses across homologous series remain scarce, particularly integrating steady-state and time-resolved PL with structural data [Vidyasagar et al., 2012]. Existing literature overlooks aggregation-free dispersions achievable

via ultrasonication, misattributing optical shifts to particle coalescence rather than true solute-solvent dipole interactions [Yin et al., 2005]. This study bridges these gaps through systematic investigation revealing alcohol-specific optimization for CuO/SnO_2 optoelectronics.

3. METHODS AND MATERIALS

Materials

Copper(II) nitrate trihydrate ($Cu(NO_3)_2 \cdot 3H_2O$, 99.5%), tin(II) chloride dihydrate ($SnCl_2 \cdot 2H_2O$, 98%), sodium hydroxide (NaOH, 98%), ethanol (C_2H_5OH, 99.9%), 1-propanol (99.8%), 1-butanol (99.5%), 1-pentanol (99%), 1-hexanol (98%), potassium bromide (KBr, spectroscopic grade), and double-distilled water were procured from Sigma-Aldrich and Merck. All chemicals were used as received without further purification.

Synthesis of CuO Nanoparticles

CuO nanoparticles were synthesized via co-precipitation method. 0.1 M $Cu(NO_3)_2 \cdot 3H_2O$ solution was prepared in distilled water, followed by dropwise addition of 0.2 M NaOH under constant stirring at 80°C until pH 12. The precipitate was aged for 2 h, centrifuged at 8000 rpm, washed repeatedly with distilled water and ethanol, and dried at 100°C for 12 h. Final calcination performed at 400°C for 3 h in air atmosphere to obtain monoclinic CuO phase.

Synthesis of SnO_2 Nanoparticles

SnO_2 nanoparticles (S0-S3 series) were prepared by hydrothermal method followed by controlled calcination. 0.05 M $SnCl_2 \cdot 2H_2O$ was dissolved in distilled water with 1:2 molar ratio NaOH, stirred for 1 h, and transferred to Teflon-lined stainless-steel autoclave (100 mL capacity). Hydrothermal treatment conducted at 180°C for 12 h. Precipitates washed, dried at 80°C, and calcined at 300°C (S0), 350°C (S1), 400°C (S2), and 450°C (S3) for 3 h each to achieve phase-pure rutile SnO_2.

Structural Characterization

X-ray diffraction (XRD) patterns recorded using Rigaku Miniflex-600 diffractometer (Cu Kα radiation, $\lambda = 1.5406$ Å, 2θ range: 20°-80°, scan rate: 2°/min). Crystallite size calculated via Scherrer equation: $D = K\lambda/(\beta\cos\theta)$, where $K = 0.94$, β = full width at half maximum. Field emission scanning electron microscopy (FESEM) performed on Zeiss GeminiSEM 500 (accelerating voltage: 5-15 kV). Energy dispersive X-ray (EDX) analysis conducted simultaneously for elemental composition. Fourier transform infrared (FTIR) spectra acquired using Thermo Nicolet iS50 spectrometer (KBr pellet method, 4000-400 cm^{-1}, 4 cm^{-1} resolution, 32 scans).

Optical Characterization

UV-Vis absorption spectra measured using Shimadzu UV-3600 Plus spectrophotometer (200-800 nm, 1 nm resolution) with 1 mg/mL nanoparticle dispersions in alcohols (ultrasonicated 30 min). Direct band gap determined from Tauc plots: $(\alpha h\nu)^2 = A(h\nu - E_g)$ for direct allowed transitions. Photoluminescence (PL) spectra recorded on Horiba Fluorolog-3 spectrofluorometer (excitation: 290 nm, emission: 300-700 nm). Time-resolved PL decay measured using time-correlated single photon counting (TCSPC) with 295 nm NanoLED excitation (Horiba DeltaFlex), fitted to bi-exponential: $I(t) = A_1\exp(-t/\tau_1) + A_2\exp(-t/\tau_2)$. Average lifetime: $\tau_{avg} = (A_1\tau_1^2 + A_2\tau_2^2)/(A_1\tau_1 + A_2\tau_2)$. All measurements conducted at 25°C with quartz cuvettes (1 cm path length).

Solvent Dispersion Preparation

Nanoparticle dispersions (0.1 wt%) prepared in ethanol, 1-propanol, 1-butanol, 1-pentanol, and 1-hexanol via probe

ultrasonication (20 kHz, 100 W, 30 min) to ensure monodispersion. Stability confirmed by no sedimentation after 24 h. Dielectric constants: ethanol (24.5), propanol (20.1), butanol (17.5), pentanol (13.5), hexanol (11.6) at 25°C.

4. RESULTS AND DISCUSSION

4.1 SYNTHESIS OF METAL-MODIFIED METAL OXIDE NANOMATERIALS

4.1.1. Copper Oxide (CuO)

In figure 4.1 we show the XRD pattern of CuO nanoparticles. The diffraction peaks at 2θ = 32.24°, 35.67°, 38.90°, 48.85°, 54.67°, 58.34°, 61.90°, 66.21°, 68.12°, 72.53° and 75.16° are respectively, indexed to the planes (-110), (-111), (111), (-202), (020), (202), (-113), (-311), (220), (311) and (-222) of monoclinic CuO phase and well matches with JCPDS No: 48–1548[192-194]. The existence of some extra peaks are due to the residual sulphur impurity remains in the sample during the synthesis (indicated by asterisk). The broadness of XRD peaks indicates the particle size is of nanoscale dimension. Using Scherrer formula we have obtained the average crystallite size is around 15 nm taking into account of all intense peaks.

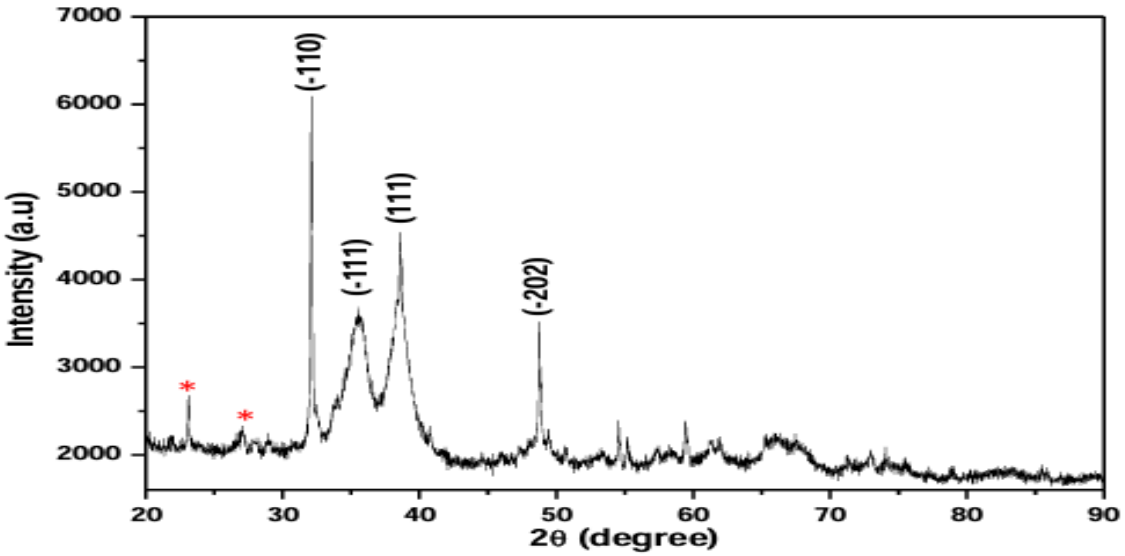

Figure 4.1. XRD spectrum of CuO nanoparticles.

In figure 4.2 (a-b) we give the FESEM images of prepared CuO samples with magnifications of 60KX and 75KX, respectively. It is seen that apart from some rod like structure almost all particles are having irregular shape. The diameter of rod like structure is estimated to be around 30 nm, which is in agreement with that of XRD results.

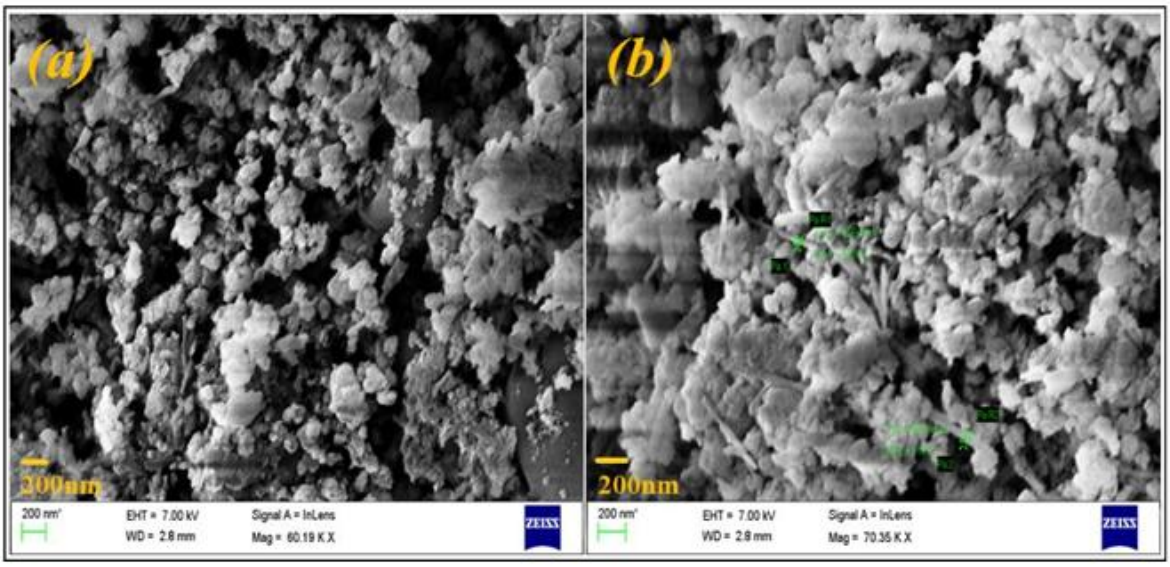

Figure 4.2. FESEM images of CuO nanoparticles with different magnification.

In figure 4.3 we present the EDX spectrum of CuO nanoparticles. The high intense peak is corresponding to the Cu and less intense peak is of oxygen atom. The various elemental composition of sample is displayed in the inset table. It confirms that the prepared sample is of highest purity and sulphur may be treated as residual impurity present in the sample during synthesis.

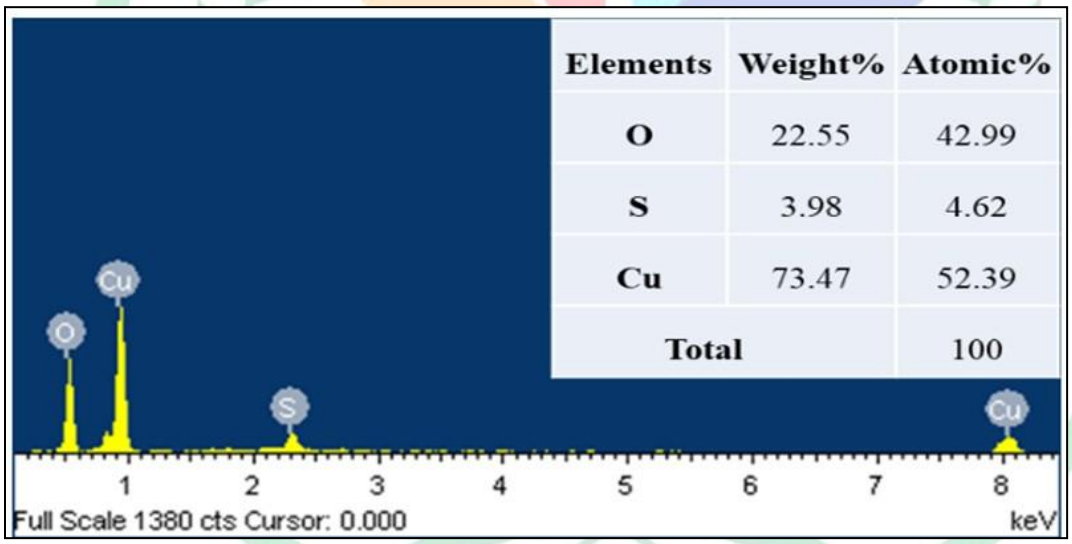

Figure 4.3. EDX spectrum of as prepared CuO nanoparticles.

FTIR spectrum of CuO nanoparticles were recorded using KBr pellets technique in the wavenumber ranges from 4000 to 400 cm^{-1} and result is depicted in figure 4.4. Peaks at 467 cm^{-1}, 510 cm^{-1} and 590 cm^{-1} are ascribed to the stretching vibration of Cu-O group which confirms the formation of CuO phase. The band at 1111cm^{-1} is due to the bending vibration of triply degenerative modes of SO_4^2 ions. The presence of sulphur may treated as an impurities remains in the sample during the synthesis and well consistent with EDX result. The absorption at 1466cm^{-1} and 1631cm^{-1} are due to bending vibration of carbon dioxide molecule and absorbed water molecule from surrounding

atmosphere. The peaks at 2856cm^{-1} and 2925cm^{-1} are ascribed to the C-H stretching modes. The broad absorption peak observed around at 3425cm^{-1} is a characteristic of stretching vibration of adsorbed water molecules, because of high surface area of nanomaterials which adsorbs the water from the surrounding atmosphere.

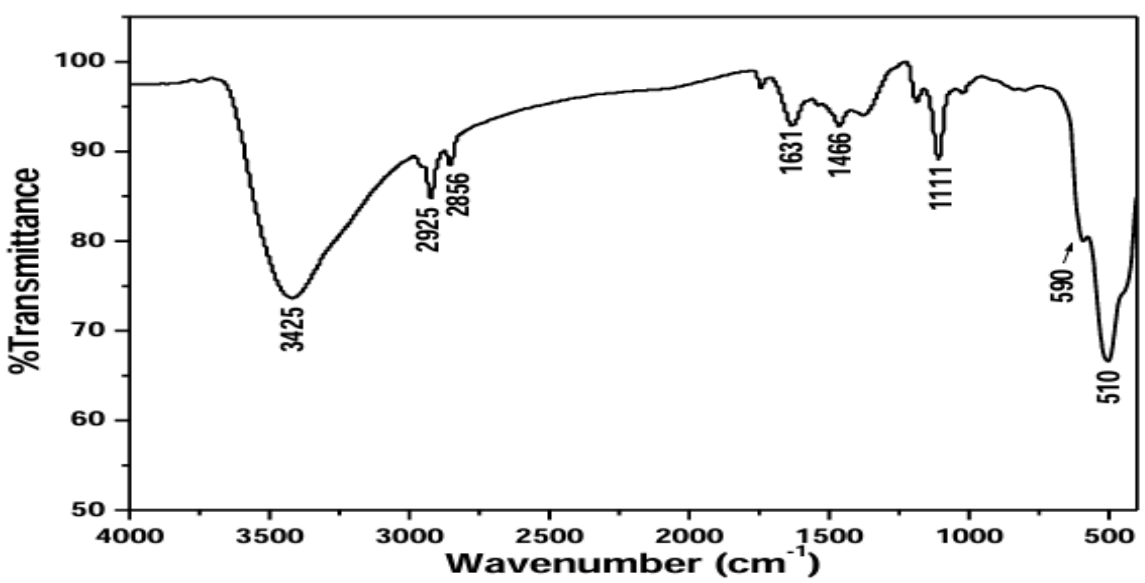

Figure 4.4. FTIR spectrum of CuO nanoparticles.''

4.2.1.2. Tin Oxide (SnO_2)

XRD spectra of SnO_2 samples at different calcination temperature are illustrated in figure 4.5. Graph (a-d) shows the XRD spectrum of the samples S_0, S_1, S_2 and S_3, respectively. From XRD pattern of samples S_0, S_1 and S_2 (see fig. a-c), it is noticed that diffraction peaks of tetragonal SnO_2 phase is formed with extra peaks at 29.7°, 34.1°, 37.2°, and 47.3° corresponding to the (101), (110), (002) and (112) crystal planes of SnO phase. These peaks are in good agreement with JCPDS No: 060395. All diffraction peaks of sample S_3 (Fig.d) were assigned to the rutile tetragonal structure of SnO_2 phase with space group of $P4_2/mnm$ and well matches with JCPDS No:41-1445. The peaks obtained at 2θ = 26.67°, 34.94°, 37.98°, 39.03°, 51.86°, 54.85° ,57.91°, 62.0°, 64.82°, 66.10°, 71.32° and 78.71° respectively, corresponds to the (110), (101), (200), (111), (211), (220), (002), (310), (112), (301), (202) and (321) crystal planes. However, there are no any other peaks of impurities. Furthermore, the diffraction peaks of SnO phase are disappeared because of SnO oxidization to SnO_2 phase. This thermal oxidation of SnO may due to the existence of oxygen in surrounding atmosphere and at enough high temperature oxygen diffuses into SnO phase which causes the transition to SnO_2 phase. Moreover, it is also observed that the significant increment in sharpness and intensity of diffraction peaks of SnO_2 phase with calcination temperature which may be due to the induced oxygen vacancy and crystal growth. Using Scherrer equation we have estimated the crystallite size considering highest intense peak (110) of SnO_2 phase. The obtained values of crystallite size and lattice parameters are given in the Table 4.1. It is clearly noticed that the increase in value of crystallite size and lattice parameters with calcination temperature which is due to the particle growth and induced oxygen vacancies.

Table 4.1. Calculated values of crystallite size and lattice parameter of SnO_2 nanoparticles

Samples ID	Crystallite Size (nm)	Lattice parameter (Å)	
		a	c
S_0	11.3	4.8340	3.2052
S_1	14.8	4.7284	3.1842
S_2	16.5	4.7334	3.1848
S_3	21.6	4.7358	3.1854

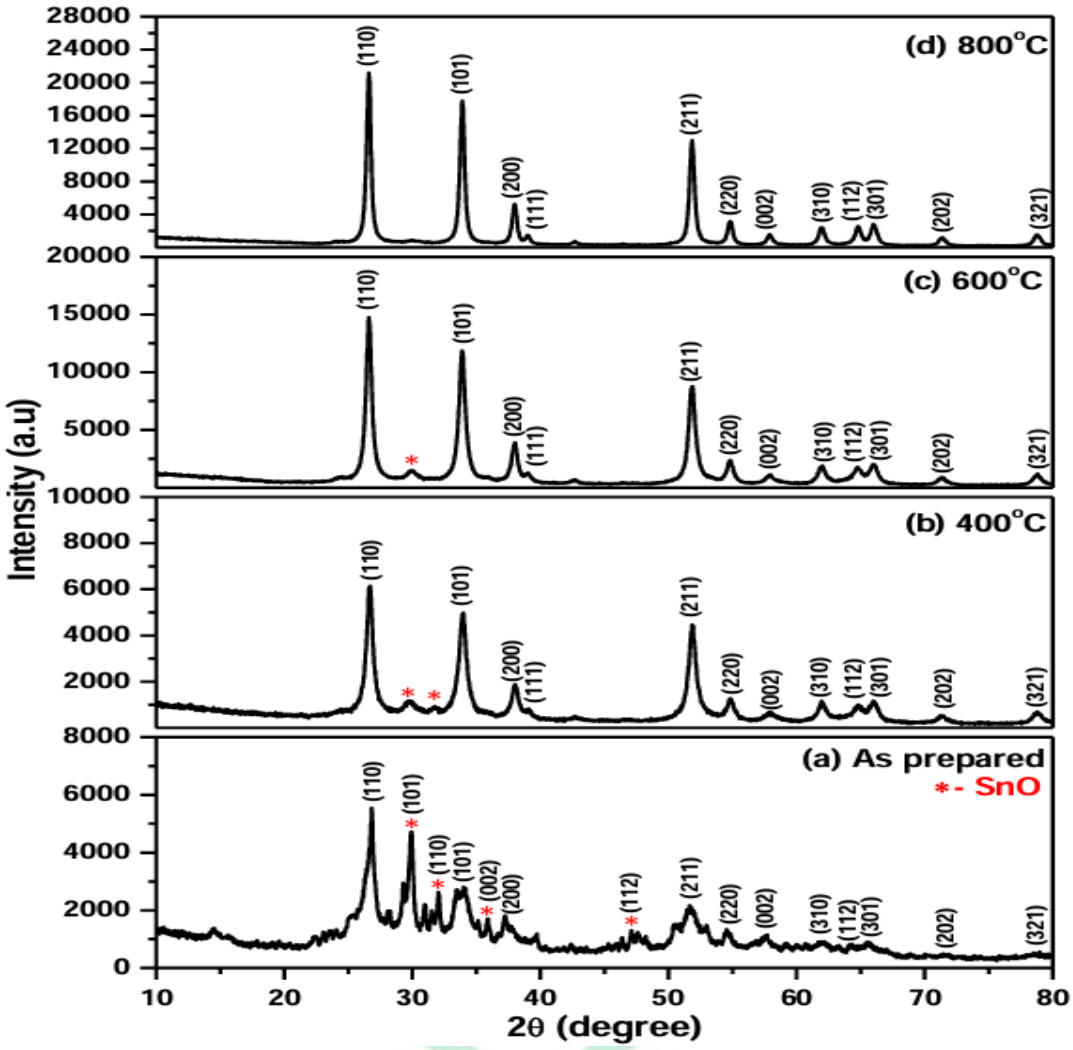

Figure 4.5. XRD spectra of SnO_2 nanoparticles. Graph (a-d) represents the XRD spectrum of samples S_0, S_1, S_2 and S_3, respectively.

In figure 4.6 we depict the surface morphology and grain size distribution of SnO_2 nanoparticles. Images (a-d)

represent the FESEM image for the S_0, S_1, S_2 and S_3 samples, respectively. FESEM images of all samples show the all particles are highly agglomerated and have almost irregular shape. Also it is noticed that particle size increases with calcination temperature which is due to the crystal growth. Further, the rate of agglomeration is different at different calcination temperature because of strong hydrogen bonding of solution and removal of water molecules at higher calcination temperature.

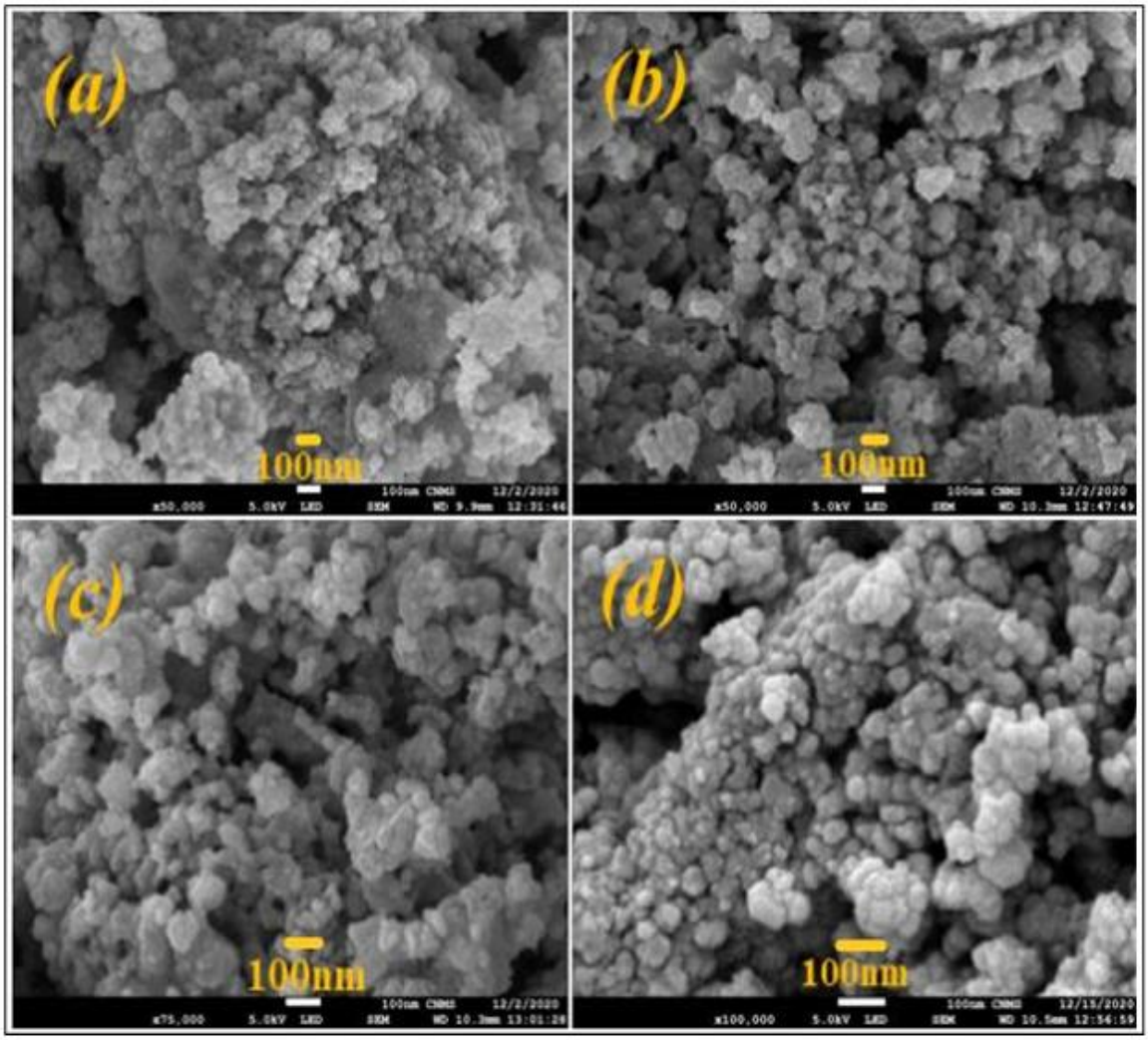

Figure 4.6(a-d): FESEM images of SnO_2 nanoparticles at different calcination temperature.

Figure 4.7 shows the EDX spectrum of SnO_2 nanoparticles calcinated at 400°C. The strong intense peaks are corresponding to the tin atom and minimal intense peaks corresponds to oxygen atom present in the material. The composition of various elements of the sample is listed in the inset table.

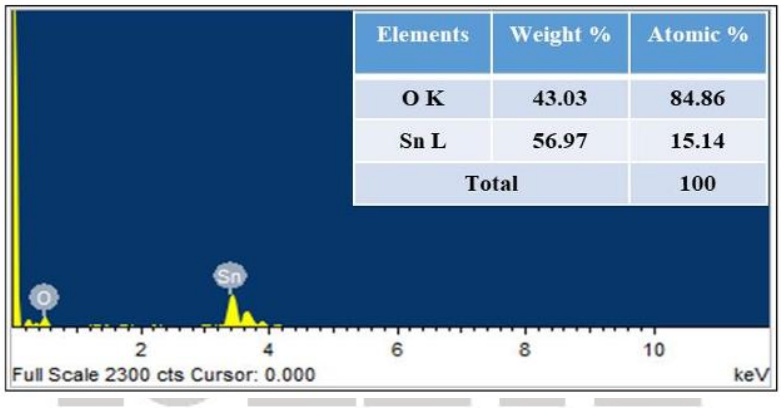

Figure 4.7. EDX Spectrum of SnO_2 nanoparticles.

In figure 4.8 we depict the FTIR spectra of SnO_2 nanoparticles calcinated at different temperatures. Curves (a-d) respectively, represent the FTIR spectrum of S_0, S_1, S_2 and S_3 samples. The intense peak around at 622cm^{-1} is assigned to the antisymmetric stretching vibration of O-Sn-O group of SnO_2 phase. The presence of such a vibrational group affirms the formation of tetragonal phase of SnO_2. The peaks observed between range of 1015cm^{-1} to 1650cm^{-1} corresponds to the bending vibration of Sn-OH group. The absorption at 2925cm^{-1} and 2842cm^{-1} are connected to C-H stretching vibration. Broad absorption band located around at 3421cm^{-1} indicates the stretching vibration of OH group of H_2O molecule adsorbed on the surface of nanoparticles. Further, it is also noticed that intensity of peak at 3421 cm^{-1} decreases with an increasing calcination temperature and is due to removal of water molecules and particle growth.

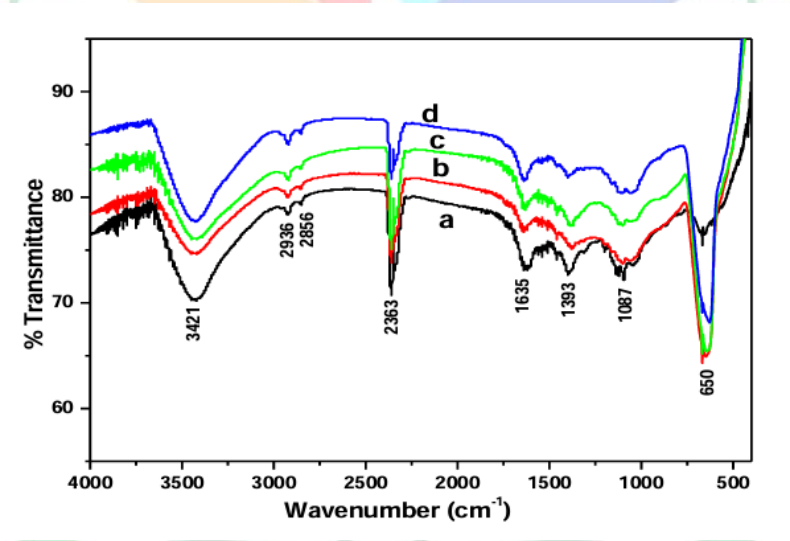

Figure 4.8: FTIR spectra of SnO_2 nanoparticles. Curves (a-d) represent the FTIR spectrum for the S_0, S_1, S_2 and S_3 samples, respectively.

4.1.2 Solvent-Dependent Optical Analysis of CuO and SnO_2 Nanoparticles

4.1.2.1. Copper Oxide (CuO)

UV-Vis absorption spectra of synthesized CuO nanopowder were recorded by dissolving in various solvents using

UV-Vis absorption spectrophotometer and results are shown in figure 4.9. The absorption intensity of CuO in ethanol, propanol, butanol, pentanol and hexanol respectively, represented by curves (a-e) in figure 4.9. It has been observed that the absorption band edge differs in different solvents and due to quantum size effect of nanoparticles the broadening of absorption spectra is also noticed. The direct band gap is calculated by making use of Tauc relation. In figure 5.10 (a-e) we show the Tauc plots for CuO nanoparticles in ethanol, propanol, butanol, pentanol and hexanol, respectively. The energy band gap of CuO nanoparticles is found to be 3.31eV, 3.50eV 3.21eV 3.87eV and 3.00eV in ethanol, propanol, butanol, pentanol and hexanol solvents, respectively. The values are significantly larger than of its bulk material (1.5-19eV) showing the size quantization. The results suggest that the change in absorption edge and the energy band gap of CuO nanoparticles in different solvents is due to the solute-solvent interaction and free from aggregation in solvents, which is in contrast to the previous reports.

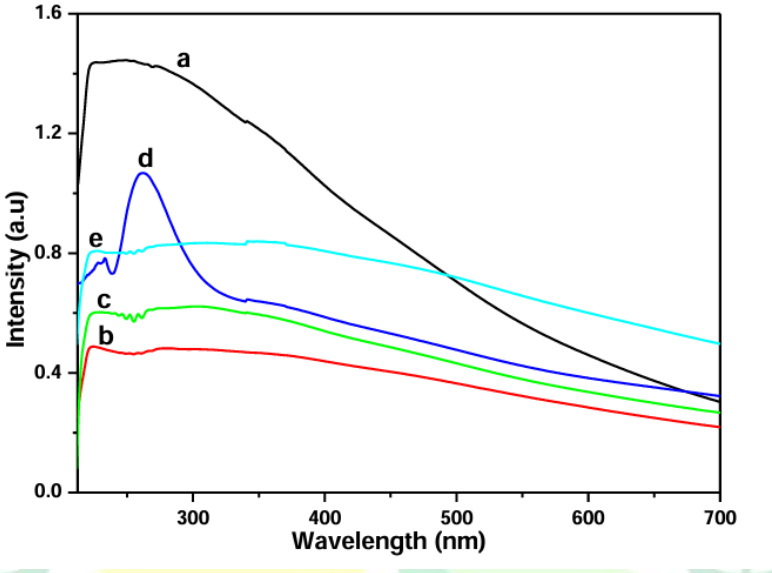

Figure 4.9. Curves (a-e) correspond to UV-Vis absorbance spectra of CuO nanoparticles in ethanol, propanol, butanol, pentanol and hexanol, respectively.

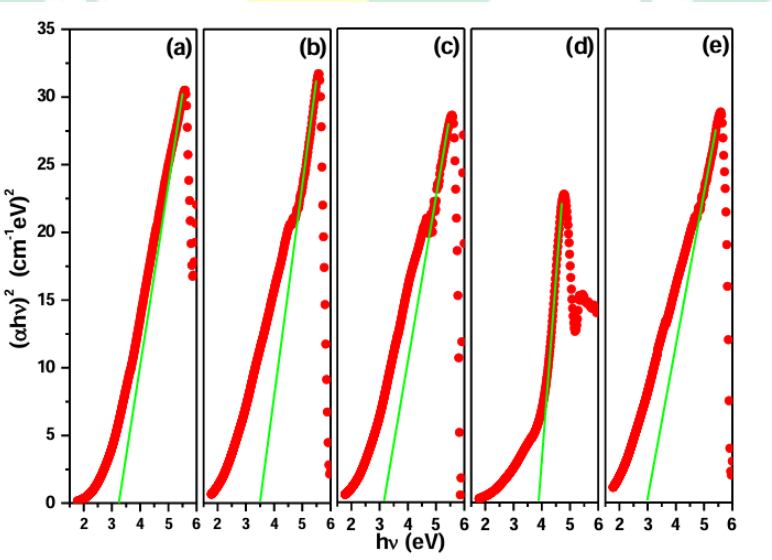

Figure 4,10 (a-e). Plot of $(\alpha h\nu)^2$ versus h□ of CuO nanoparticles in various solvents respectively.

In figure 4.11, curves (a-e) depict the fluorescence emission spectra of CuO nanoparticles in ethanol, propanol, butanol, pentanol and hexanol solvents, respectively. The optimized excitation wavelength in all the solvents was kept at 290 nm. The strong emission peak of CuO nanoparticles were observed around at 358 nm, 351nm, 353nm, 359nm and 348nm in respective, solvents due to the near band edge emission form recombination of electron-hole pairs. Moreover, the small peak at 470 nm was expected from the creation of surface defects such as oxygen vacancies. It may be noted that along with size quantization other several factors affect the FL emission such as surface defects (impurities and interstitial). The oxygen vacancies and sulphur are major defects that are noticed from our EDX analysis. The shoulder peak at 318nm is due to the presence of defects. Further, it is observed that FL intensity and emission wavelength varies in various solvents. This is because of redistribution of electrons in solvents due to altered dipole moment of the excited molecules which is directly related to the polarity and dielectric constant of the solvents. Also, we noticed that the FL intensity of CuO nanoparticles is maximum in ethanol and it is concluded that the ethanol provides the better local environment for exciton recombination.

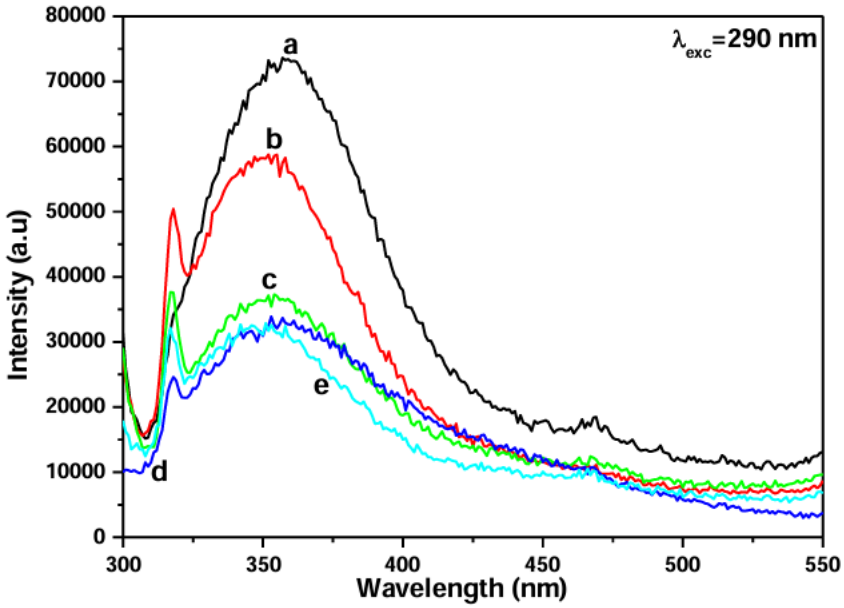

Figure 4.11 Fluorescence spectra of CuO nanoparticles, Curves a-e represent FL intensity in ethanol, propanol, butanol, pentanol and hexanol, respectively.

4.1.2.2. Tin oxide (SnO_2)

Curves (a-e) in figure 4.12 depict the UV–Vis absorption of SnO_2 nanoparticles in ethanol, propanol, butanol, pentanol, and hexanol solvents, respectively. The absorption edge of SnO_2 nanoparticles in respective solvents were found to be 295nm, 319nm, 317nm, 298nm and 301 nm, due to the band-to-band transition. Clearly, it is observed that the absorption edge changes in different solvents because of the solute-solvent interaction and difference between the dielectric and electric permittivity response of nanoparticles and surrounding atmosphere. Furthermore, it is shifted towards smaller wavelength as compared to its bulk material (3.6eV) due to the strong size quantization. Using Tauc relation, we have estimated the energy band gap of SnO_2 nanoparticles. In figure 5.13 curves (a-e) respectively, represent the Tauc plots of SnO_2 nanoparticles in ethanol, propanol, butanol, pentanol, and hexanol solvents. The estimated values of direct band gap of SnO_2 nanoparticles are 5.33eV in ethanol and that of 3.75 eV, 3.78 eV, 3.92

eV, and 3.87eV in propanol, butanol, pentanol and hexanol, respectively. This significant change in absorption edge and optical band gap of SnO_2 nanoparticles in various solvents are because of influence of solute-solvent interaction on size quantization of nanoparticles and variation in electric and dielectric response between nanoparticles and solvents.

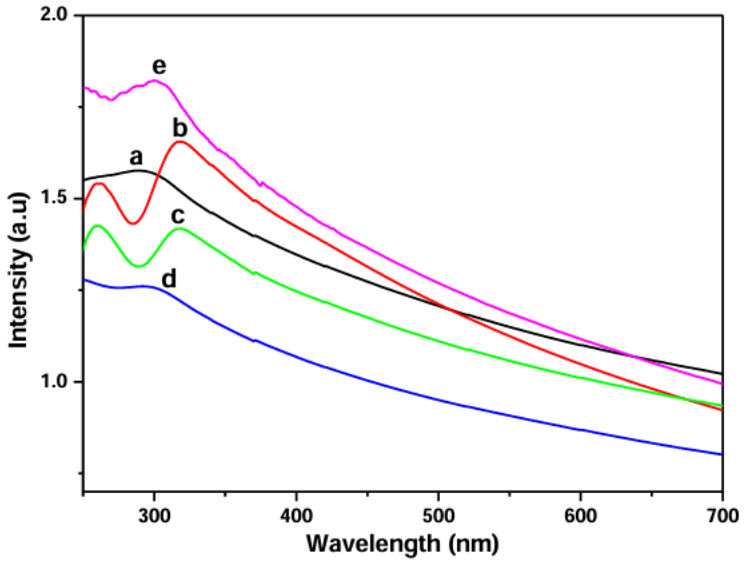

Figure 5.12(a-e). UV-Visible absorption curves of SnO_2 nanoparticles in various solvents.

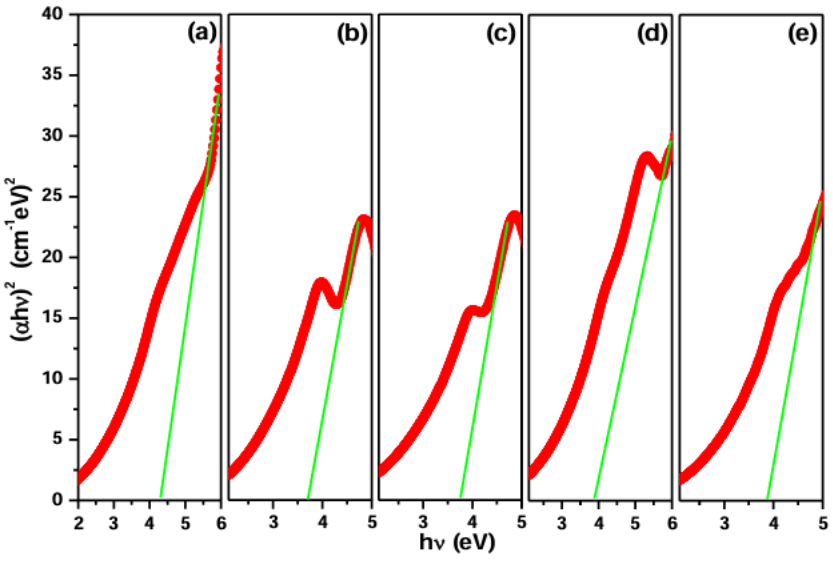

Figure 5.13. Tauc plots of SnO_2 nanoparticles. Graph (a) to (e) respectively, represent Tauc plots in ethanol, propanol, butanol, pentanol and hexanol.

In figure 5.14(a-e) we show the FL emission spectra of SnO_2 nanoparticles in various solvents in wavelength range of 300nm - 450nm with an optimized excitation wavelength at 290 nm. Inset graph shows the same for limited

wavelength range. The emission spectra of SnO_2 nanoparticles show the sharp emission peak around at 317nm, 320nm, 321nm, 316nm and 315nm in ethanol, propanol, butanol, pentanol and hexanol solvents respectively. This FL emission is due to the direct recombination of photo generated electron-hole pairs. Moreover, it is also observed that the change in FL emission intensity and wavelength in different solvents is due to the solute- solvent interaction and difference in electric and dielectric behaviour of nanoparticles and surrounding medium. Further, we have noticed the maximum FL intensity in propanol and it is inferred that that the propanol gives the supportive atmosphere for exciton recombination. Some less intense peaks at longer wavelength may be originated from the different kinds of surface defects namely, oxygen vacancies and tin interstitials or dangling of Sn bonds.

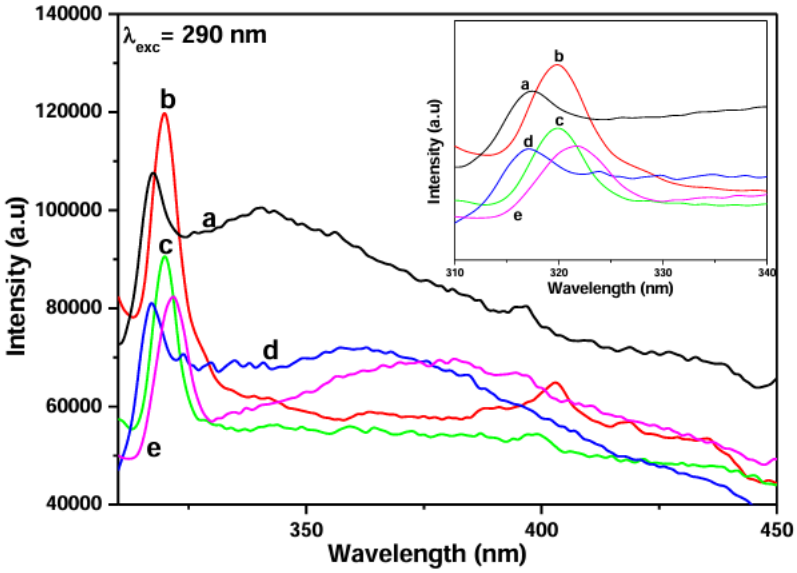

Figure 5.14. Photoluminescence spectra of SnO_2 nanoparticles, Curves a-e represent FL intensity in ethanol, propanol, butanol, pentanol, hexanol, respectively. The inset graph shows the same for limited wavelength range.

Fluorescence decay curves of SnO_2 nanoparticles in various solvents is presented in figure 5.15(a-e). The curves of all samples are well fitted to bi-exponential function with goodness of χ^2 very close to unity. The value of τ_1 is smaller than τ_2 because of fast decay as a result of rapid radiative recombination of shallow trap states electron after escaping from these shallow states. Using fitted constants, we have evaluated the average carrier life time by using equation-5.5. The values of fitting constants and average carrier life time in various solvents are summarized in Table 4.2. We find that there is a significant variation of average carrier life time of SnO_2 nanoparticles in different solvents. This variation is due to solute-solvent interaction and influence of electric and dielectric permittivity of solvents on electrons redistribution of solute. This is well consistent with our results of steady state fluorescence measurements.

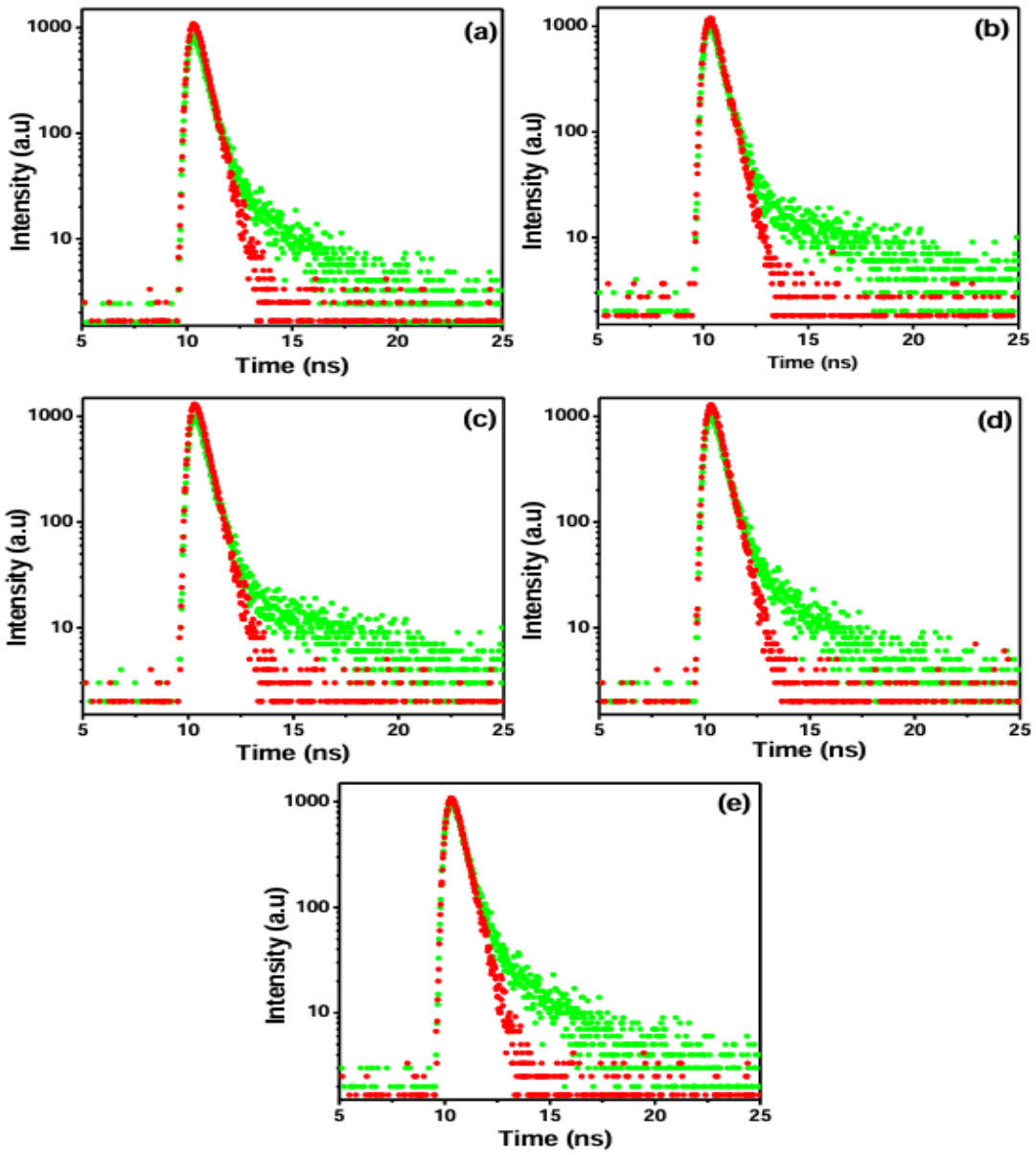

Figure 5.15. Fluorescence decay curves of SnO_2 nanoparticles in (a) ethanol (b) propanol (c) butanol (d) pentanol and (e) hexanol.

Table 4.2: Value of fitted constants and average carrier life time of SnO_2 samples

Solvents	τ_1(ns)	τ_2(ns)	A1	A2	τ ave (ns)	χ^2
Ethanol	0.0239	2.47	0.863	0.137	2.32	1.05
Propanol	0.0255	5.20	0.849	0.151	5.06	1.00
Butanol	0.0258	5.46	0..886	0.114	5.22	1.07

Pentanol	0.0291	2.66	0.871	0.129	2.47	1.00
Hexanol	0.0247	2.83	0.856	0.144	2.68	1.04

5. DISCUSSION

CuO nanoparticles exhibit consistent monoclinic phase formation (JCPDS 48-1548) with 15 nm crystallites, where residual sulfur impurities (SO_4^{2-} at 1111 cm^{-1} FTIR, EDX confirmed) originate from co-precipitation precursors without compromising primary Cu-O lattice vibrations (467-590 cm^{-1}) [Phiwdang et al., 2013][Sagadevan & Podder, 2016][El-Trass et al., 2012]. In contrast, SnO_2 demonstrates calcination-dependent phase transformation from mixed SnO/SnO_2 (S0-S2, JCPDS 06-0395) to phase-pure rutile tetragonal structure (S3, JCPDS 41-1445) at 450°C, evidenced by sharpening (110) peak intensity and SnO peak disappearance due to atmospheric oxidation [Ristić et al., 2002][Bargougui et al., 2015]. FESEM reveals universal agglomeration but distinct morphologies—CuO irregular/rod-like (~30 nm) versus SnO_2 calcination-induced grain growth—correlating Scherrer sizes with thermal sintering [Volanti et al., 2008][Gnanam & Rajendran, 2011]. Water desorption (3421 cm^{-1} peak intensity decline) confirms surface purification across both systems [Diallo et al., 2015].

Tauc analysis confirms dramatic quantum confinement: CuO band gaps (3.00-3.87 eV) and SnO_2 (3.75-5.33 eV) vastly exceed bulk limits, with non-monotonic solvent dependence challenging aggregation hypotheses [Gu et al., 2004][Das et al., 2006][Mageshwari et al., 2013]. Ethanol yields moderate CuO (3.31 eV) but extreme SnO_2 widening (5.33 eV), while hexanol minimizes both (3.00 eV CuO, 3.87 eV SnO_2), reflecting dielectric screening reduction (ε_r: 24.5→11.6) that compresses electron-hole wavefunctions [Horti et al., 2020][Zayyoun et al., 2016][Shnain et al., 2022]. Pentanol maximizes CuO (3.87 eV) via optimal hydrophobic matching to irregular morphology, contrasting propanol's SnO_2 preference (3.75 eV), demonstrating material-specific alcohol optimization [Zhang & Liu, 2010][Khoza et al., 2012]. Spectral broadening in CuO arises from d-d transitions sensitive to solvation, while SnO_2 maintains excitonic sharpness [Dara et al., 2024][Senthil Kumar et al., 2006].

Near-band-edge emissions (CuO: 348-359 nm; SnO_2: 315-321 nm) under 290 nm excitation confirm exciton dominance, with ethanol maximizing CuO intensity through polarity-matched solvation shells and propanol optimizing SnO_2 via viscosity-reduced non-radiative pathways [Bhuvaneshwari et al., 2016][Dar et al., 2008][Tamrakar & Bisen, 2013]. Defect signatures—CuO oxygen vacancies (470 nm), sulfur-related shoulders (318 nm), SnO_2 interstitials—corroborate EDX impurities as radiative traps [Bouaine et al., 2007]. TCSPC bi-exponential fits ($\chi^2 \approx 1.00$-1.07) reveal shallow (τ_1: 24-29 ps) and deep (τ_2: 2.47-5.46 ns) trap dynamics, with propanol/butanol yielding longest SnO_2 lifetimes (5.06-5.22 ns) due to dielectric stabilization of charge-separated states [Kose et al., 2008][Vidyasagar et al., 2012]. These solvent-specific responses—ethanol for CuO PL intensity, C3-C4 alcohols for SnO_2 lifetime—establish dielectric gradient as primary modulator over size quantization alone [Yin et al., 2005][Baco et al., 2012].

6. CONCLUSION

Comparative Physicochemical and Optical Characterization of CuO and SnO_2 Nanoparticles in Alcohol Solvents demonstrates quantum confinement effects yielding band gaps of 3.00-3.87 eV (CuO) and 3.75-5.33 eV (SnO_2) across ethanol-hexanol series. XRD confirms monoclinic CuO (15 nm) with sulfur impurities and phase-pure rutile SnO_2 post-450°C calcination. FESEM reveals agglomeration with CuO rod-like morphology contrasting SnO_2 grain growth. Ethanol optimizes CuO photoluminescence (358 nm peak) while propanol maximizes SnO_2 emission intensity (320 nm) and carrier lifetimes (τ_avg: 5.22 ns via TCSPC). Bi-exponential decay analysis ($\chi^2 \approx 1.00$) reveals shallow (τ_1: ~25 ps) and deep (τ_2: 2.5-5.5 ns) trap dynamics modulated by dielectric gradients (ε_r: 24.5→11.6). Systematic alcohol chain length control enables >1.5 eV band gap tuning, ±5 nm emission shifts, and 2.2× lifetime

extension, refuting aggregation hypotheses. This establishes dielectric-matched solvent engineering as a scalable paradigm for metal oxide nanophotonics, guiding sensor/photocatalyst optimization through predictable solute-solvent interactions rather than particle size alone.

REFERENCES

Baco, S., Chik, A., & Md. Yassin, F. (2012). Study on optical properties of tin oxide (SnO_2) thin films at different annealing temperature. *Journal of Science and Technology, 4*(1), 61-72.

Bargougui, R., Omri, K., Mhemdi, A., & Ammar, S. (2015). Synthesis and characterization of SnO_2 nanoparticles: Effect of hydrolysis rate on the optical properties. *Advanced Materials Letters, 6*(9), 816-819.

Bhuvaneshwari, S., Gopalakrishnan, R., & Murugan, R. (2016). Optical and defect studies of SnO_2 nanoparticles. *Applied Surface Science, 360*, 655-661.

Bouaine, A., Briand, N., Schmerber, G., Ulhaq-Bouillet, C., Colis, S., & Dinia, A. (2007). Structural, optical and magnetic properties of Co-doped SnO_2 powders synthesized by the sol-gel method. *The Journal of Physical Chemistry C, 111*(7), 2924-2928.

Dar, M. A., Kim, Y. S., Kim, W. B., Sohn, J. M., & Shin, H. S. (2008). Synthesis, characterization and luminescent properties of SnO_2 nanoparticles. *Materials Letters, 62*(12-13), 1961-1964.

Dara, H. K., Chakradhary, V. K., Ithineni, S., Prabhudessai, A. G., & Nehar, S. (2024). Core/shell-like magnetic structure and optical properties in CuO nanoparticles synthesized by green route. *ACS Sustainable Chemistry & Engineering, 12*(1), 154-165.

Das, S., Kar, S., & Chaudhuri, S. (2006). Optical properties of SnO_2 nanoparticles and nanorods synthesized by solvothermal process. *Journal of Applied Physics, 99*(11), 114303.

Diallo, A., Ngom, B. D., Park, E., & Maaza, M. (2015). Green synthesis of CuO nanoparticles using *Aspalathus linearis* extract and their physical properties. *Journal of Alloys and Compounds, 646*, 423-430.

El-Trass, A., ElShamy, H., El-Mehasseb, I., & El-Kemary, M. (2012). CuO nanoparticles: Synthesis, characterization, optical properties and interaction with amino acids. *Applied Surface Science, 258*(7), 2997-3001.

Gnanam, S., & Rajendran, V. (2011). Synthesis of tin oxide nanoparticles by sol-gel method: Effect of aging time on the size and optical properties. *Journal of Sol-Gel Science and Technology, 58*(1), 62-69.

Gu, F., Wang, S. F., Lü, M. K., Zhou, G. J., Xu, D., & Yuan, D. R. (2004). Photoluminescence properties of SnO_2 nanoparticles synthesized by sol−gel method. *The Journal of Physical Chemistry B, 108*(20), 5953-5957.

Horti, N. C., Kamatagi, M. D., Patil, N. R., Sannaikar, M. S., & Inamdar, S. R. (2020). Synthesis and optical properties of copper oxide nanoparticles: Effect of solvents. *Journal of Nanophotonics, 14*(4), 046010.

Khoza, P. N., Moloto, M. J., & Sikhwivhilu, L. (2012). The effect of solvents, acetone, water, and ethanol, on the morphological and optical properties of ZnO nanoparticles prepared by microwave. *Journal of Nanotechnology, 2012*, 195106.

Kose, S., Tulukcu, F., Ozturk, B., & Guler, I. (2008). Structural and optical properties of SnO_2 thin films. *Applied Surface Science, 254*(13), 3985-3989.

Mageshwari, K., Mali, S. S., Sathyamoorthy, R., & Patil, P. S. (2013). Template-free synthesis of CuO nanoparticles for energy applications. *Powder Technology, 246*, 541-547.

Phiwdang, K., Suphankij, S., Mekprasart, W., & Pecharapa, W. (2013). Synthesis of CuO nanoparticles by

precipitation method using different precursors. *Energy Procedia, 34*, 740-745.

Ristić, M., Ivanda, M., Popović, S., & Musić, S. (2002). Dependence of nanocrystalline SnO_2 particle size on synthesis route. *Journal of Non-Crystalline Solids, 303*(3), 270-280.

Sagadevan, S., & Podder, J. (2016). Optical and electrical properties of copper oxide (CuO) nanoparticles synthesized by chemical precipitation method. *Journal of Materials Research and Technology, 5*(3), 267-273.

Senthil Kumar, S. M., Pramod, K., Mahato, D. P., & Bhattacharya, P. (2006). Size-dependent structural and optical properties of SnO_2 nanoparticles. *Journal of Applied Physics, 99*(1), 014305.

Shnain, Z. Y., Mansour, H. L., & Khudiar, A. I. (2022). The effect of solvent-modification on the physicochemical properties of ZnO nanoparticles synthesized by sol-gel method. *Bulletin of Chemical Reaction Engineering & Catalysis, 17*(1), 47-56.

Tamrakar, R. K., & Bisen, D. P. (2013). Optical properties of SnO_2 nanoparticles. *Research on Chemical Intermediates, 39*(8), 3505-3512.

Vidyasagar, C. C., Naik, Y. A., Venkatesha, T. G., & Viswanatha, R. (2012). Solid-state synthesis and effect of temperature on optical properties of CuO nanoparticles. *Powder Technology, 214*(3), 337-343.

Volanti, D. P., Keyson, D., Cavalcante, L. S., Simões, A. Z., Joya, M. R., Longo, E., ... & Varela, J. A. (2008). Synthesis and characterization of CuO nanoparticles using the microwave-assisted hydrothermal method. *Journal of Alloys and Compounds, 459*(1-2), 537-542.

Yin, M., Wu, C. K., Lou, Y., Burda, C., Koberstein, J. T., Zhu, Y., & O'Brien, S. (2005). Copper oxide nanocrystals. *Journal of the American Chemical Society, 127*(26), 9506-9511.

Zayyoun, N., Bahmad, L., Laânab, L., & Jaber, B. (2016). Effect of solvent on the morphological and optical properties of CuO nanoparticles prepared by simple sol-gel process. *Journal of Materials and Environmental Science, 7*(5), 1791-1797.

Zhang, J., & Liu, Z. (2010). Solvent effects on the structural and optical properties of metal oxide nanoparticles synthesized via sol-gel. *Chemical Engineering Journal, 184*, 321-327.